Immobilization of graphene-derived materials at gold surfaces: Towards a rational design of protein-based platforms for electrochemical and plasmonic applications

Emiliano N. Primo [a, b], Soledad Bollo [c, *], María D. Rubianes [a, b, **], Gustavo A. Rivas [a, b, ***]

[a] INFIQC (CONICET), Haya de la Torre s/n, Ciudad Universitaria, X5000HUA, Córdoba, Argentina
[b] Departamento de Fisicoquímica, Facultad de Ciencias Químicas, Universidad Nacional de Córdoba, Ciudad Universitaria, X5000HUA, Córdoba, Argentina
[c] Centro de Investigación de Procesos Redox (CiPRex), Advanced Center for Chronic Diseases (ACCDiS), Facultad de Ciencias Químicas y Farmacéuticas, Departamento de Química Farmacológica y Toxicológica, Universidad de Chile, 838492, Santiago, Chile

A R T I C L E   I N F O

A B S T R A C T

This work is focused on the critical analysis of the non-covalent modification of a thiolated-gold surface with different grapheneous materials and the covalent attachment of bovine serum albumin (BSA) as a model protein. The main goal was to find a relationship between the nature and amount of the grapheneous nanomaterial, the amount of immobilized protein, and the electrochemical and plasmonic properties of the resulting platforms. The characterization of the grapheneous nanomaterials (graphene oxide (GO), GO modified with chitosan (CHIT), (GO-CHIT), and chemically reduced GO-CHIT (RGO-CHIT)) was performed by using FTIR, Raman, TGA, Dynamic light scattering (DLS), UV−Vis spectroscopy and ζ-potential measurements. The characterization of the thiolated-gold surfaces modified with the different nanomaterials and BSA was performed using surface plasmon resonance (SPR), cyclic voltammetry, electrochemical impedance spectroscopy (EIS) and scanning electrochemical microscopy (SECM). The pH of the grapheneous materials dispersions demonstrated to be a critical parameter to control the assembly of the nanomaterials and the model protein at the gold surfaces and, consequently, the electroactivity and plasmonics of the resulting platforms. When using GO, the optimum pH is 8.00 while in the case of GO-CHIT and RGO-CHIT, pHs << pKa,$_{CHIT}$ are the most adequate. We demonstrated that in the case of our model system, if the detection method depends on the direct quantification of the amount of BSA immobilized at the platform (like SPR), the use of GO is the best option; while if the detection mode depends on the changes in the electrochemical response of a redox marker (like EIS), the selected grapheneous material should be RGO.

1. Introduction

Grapheneous materials, a family of nanostructures that derive from the stacking of C sp^2 lattices [1], have received considerable attention in different fields due to their multiple applications which were rocketed after 2010 Nobel Prize on Geim and Novoselov work. These applications include electronics, energy, (bio)sensing, medicine and engineering [2−6]. Graphene and graphene oxide (GO) have been used as nanosupports for a variety of biologically active agents leading to novel biocatalysts, biosensors, and drug delivery vehicles. They have been interfaced, modified and/or functionalized with synthetic and natural polymers, DNA sequences, proteins, cells and small molecules [7−12]. Particularly, the interest of using grapheneous nanostructures as building blocks for biosensors relies on their outstanding properties, namely: i) large surface area that enhance the surface loading of biomolecules; ii) excellent conductivity and small band gap that can be beneficial for conducting electrons between biomolecules; iii) tunable optical

* Corresponding author. Centro de Investigación de Procesos Redox (CiPRex), Advanced Center for Chronic Diseases (ACCDiS), Facultad de Ciencias Químicas y Farmacéuticas, Departamento de Química Farmacológica y Toxicológica, Universidad de Chile, 838492, Santiago, Chile.
** Corresponding author. INFIQC (CONICET), Haya de la Torre s/n, Ciudad Universitaria, X5000HUA, Córdoba, Argentina.
*** Corresponding author. INFIQC (CONICET), Haya de la Torre s/n, Ciudad Universitaria, X5000HUA, Córdoba, Argentina.
E-mail addresses: sbollo@ciq.uchile.cl (S. Bollo), rubianes@fcq.unc.edu.ar (M.D. Rubianes), grivas@fcq.unc.edu.ar (G.A. Rivas).

properties and high transparency; and *iv*) good biocompatibility, formation of stable aqueous suspensions, and cheap strategies for production, among others.

The immobilization of graphene-derived materials at solid substrates requires strict control not only to take advantage of their intrinsic properties but also to maximize the loading of material and to obtain reproducible and appropriate surface distributions to ensure a good analytical performance of the resulting platforms. The usual strategies for the immobilization range from simple drop-casting of a graphenoid dispersion [13–16] to hydrophobic/specific/electrostatic-mediated layer-by-layer (LBL) self-assembly [17] or covalent tethering to previously derivatized substrates [15,18,19].

Different surfaces modified with grapheneous materials have been successfully used for the development of (bio)sensors following diverse protocols [6,20,21]; however, most of the reported studies have been focused on the analytical applications of the proposed grapheneous-modified surfaces rather than on a critical discussion about the criteria for selecting a given modification scheme. There are some reports where the relationship between the immobilization of a protein and the strategy used for immobilizing the grapheneous material have been investigated. Alwarappan et al. have reported an interesting study about the influence of the number of graphene and glucose oxidase layers on the electrochemical response of the resulting platform [22]. Zhang et al. have evaluated the effect of the degree of graphene oxide (GO) reduction on the activity and amount of non-covalently immobilized enzymes [23] and have demonstrated that, upon increasing the degree of hydrophobicity of reduced graphene oxide (RGO), there is an increment in the quantity of immobilized enzyme although its activity decreases. More recently, Macwan et al. have demonstrated, through molecular dynamics/experimental studies, that no significant changes in the structure of avidine were obtained after the interaction with graphene sheets [24].

The association of biomolecules (DNA sequences, proteins) with graphene-derived nanomaterials is a booming field and is widely used as strategy for the development of electrochemical and plasmonic biosensors. In this sense, the design of simple and reproducible methodologies for the preparation of biosensors that ensures the maximum efficiency in the immobilization of the biorecognition molecule and the best analytical performance of the resulting biosensing platforms, is a critical aspect. On the other hand, the transduction mode plays a crucial role in the overall efficiency of the biosensor since the final biosensing signal will critically depend on the scheme used for the transduction. If it is indirect, it generally involves the use of a probe like in the case of electrochemical impedance spectroscopy (EIS) [25,26], and if it is direct, as in the case of surface plasmon resonance (SPR) [27,28], one usually monitor an intrinsic signal of the equipment.

In this work, we report a critical analysis about the influence of the strategy used to modify gold surfaces with GO, GO modified with chitosan (CHIT) (GO-CHIT) and chemically reduced GO-CHIT (RGO-CHIT) at Au surfaces modified with sodium 3-mercapto-1-propanesulfonate (MPS) on the covalent immobilization of a model protein, bovine serum albumin (BSA). We payed special attention on the electrochemical and optical properties of the resulting platforms and the correlation between the strategies used to immobilize the grapheneous material, the amount of BSA immobilized at each platform and the mode of transducing the signal. In the following sections we discuss the non-covalent assembly of GO, GO-CHIT and RGO-CHIT at Au modified with MPS and the electrochemical and plasmonic properties of the different platforms. The different systems were evaluated using cyclic voltammetry; electrochemical impedance spectroscopy (EIS); scanning electrochemical microscopy (SECM); UV–Vis, FTIR, and Raman

spectroscopy; surface plasmon resonance (SPR); thermogravimetry (TGA); scanning electronic microscopy (SEM) and ζ-potential/hydrodynamic radius measurements.

2. Materials and methods

2.1. Materials and chemicals

Graphene oxide (GO, aqueous dispersion 4 mg mL^{-1}) was obtained from Graphenea. Chitosan (CHIT, 20–300 cP), poly(-diallyldimethylammonium chloride) (PDDA, 60–180 cP), bovine serum albumin (BSA), sodium 3-mercapto-1-propanesulfonate (MPS), 1-Ethyl-3-(3-dimethylaminopropyl)carbodiimide (EDC), *N*-hydroxysuccinimide (NHS), glutaraldehyde (Glut) and 2-(*N*-morpholino)ethanesulfonic acid (MES) were obtained from Sigma-Aldrich. Other chemicals were reagent grade and were used without further purification. All solutions were prepared with ultra-pure water (18 MΩ cm) from a Millipore-MilliQ system.

2.2. Synthesis of GO-CHIT and RGO-CHIT conjugates

The CHIT solution (2.00 mg mL^{-1}) was prepared in a 0.100 M MES buffer pH 5.00 by sonication for 2 h in an ultrasound bath. GO (1.25 mg mL^{-1}) was then added to the polymer solution and sonicated for 2 additional hours to obtain an homogeneous dispersion. The amidation reaction (Fig. S1) was carried out by adding the coupling agents [29] EDC (0.076 M) and NHS (0.076 M) to the dispersion of GO with CHIT. The mixture was sonicated for another 2 h and then was allowed to react overnight under magnetic stirring. The purification of GO-CHIT was performed by centrifuging the mixture for 1 h at 6000 rpm, discarding the supernatant and resuspending the pellet in 0.100 M MES buffer pH 5.00. This procedure was repeated 5 times to remove all the unreacted CHIT.

RGO-CHIT was obtained by reducing GO-CHIT with excess of NaBH$_4$. The GO-CHIT and the reducing agent mixture was left to react for 24 h with the aid of a magnetic stirrer. The purification was done following the same protocol as for GO-CHIT.

2.3. Modification of gold substrates

The non-covalent immobilization of GO, GO-CHIT and RGO-CHIT was performed by LBL self-assembly at a thiol-derivatized gold substrate. The Au surface was modified by immersing for 60 min in a 2.00×10^{-2} M MPS solution (prepared in 1.60×10^{-3} M H$_2$SO$_4$ solution) and further rinsing with deionized water. The surface coverage of MPS (Γ_{MPS}) was obtained by oxidative desorption experiments performed by cyclic voltammetry [30], being $\Gamma_{MPS} = (7.89 \pm 0.02) \times 10^{-10}$ mol cm^{-2}.

Non-covalent assembly of PDDA/GO and covalent attachment of BSA (Scheme 1A). Au/MPS was immersed for 15 min in a PDDA solution (1.00 mg mL^{-1} prepared in 0.050 M phosphate buffer solution pH 7.40). After rinsing with the phosphate buffer solution, the resulting Au/MPS/PDDA platform was allowed to interact for 30 min with a 0.50 mg mL^{-1} GO dispersion. The evaluation of the protein loading capacity was performed by covalent immobilization of BSA (which served as model protein), to the carboxylate residues of GO. Au/MPS/PDDA/GO was activated with a 0.050 M EDC/NHS mixture for 20 min and then left to interact for 30 min with 1.00 mg mL^{-1} BSA solution (prepared in 0.050 M phosphate buffer solution pH 7.40).

The pH of GO dispersions was adjusted to the desired value using concentrated NaOH solution and immediately assembled at Au/MPS/PDDA.

Non-covalent assembly of GO-CHIT and RGO-CHIT and covalent attachment of BSA (Scheme 1B). As the tethered polymer CHIT is
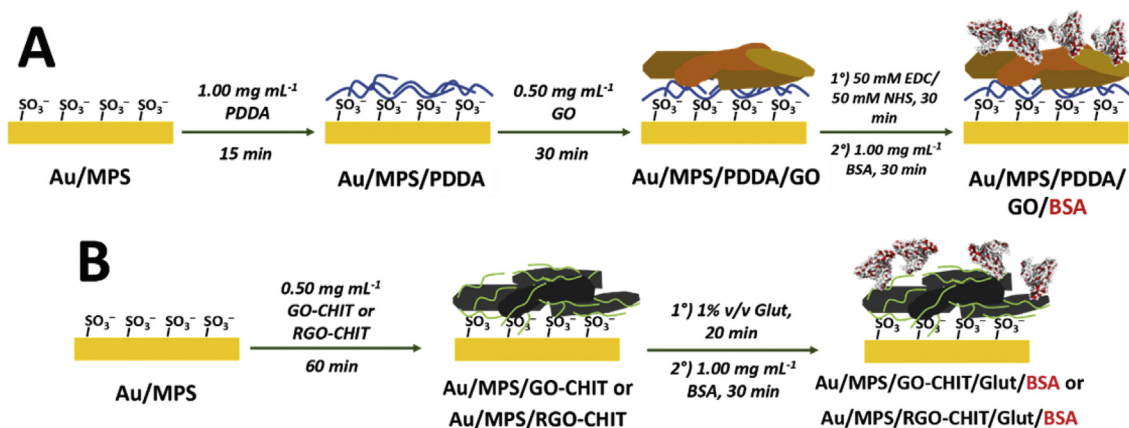
Scheme 1. Procedure for (**A**) non-covalent assembly of PPDA/GO over Au/MPS; (**B**) non-covalent assembly of RGO-CHIT (and GO-CHIT) over Au/MPS.

positively charged under the experimental conditions, both GO-CHIT and RGO-CHIT, were immobilized directly at Au/MPS by immersion for 60 min in a 0.50 mg mL^{-1} GO-CHIT or RGO-CHIT dispersion. The covalent immobilization of BSA was performed by coupling with 1.0 %v/v Glut solution (prepared in 1.0 %v/v acetic acid solution) for 20 min [31]. After rinsing the resulting platform, it was left to interact for 30 min with a 1.00 mg mL^{-1} BSA solution (prepared in 0.200 M acetate buffer solution pH 5.00).

The pH of GO-CHIT/RGO-CHIT dispersions was adjusted to the desired value using concentrated NaOH solution and immediately assembled at Au/MPS.

2.4. Apparatus and procedure

UV−Vis experiments were performed with a Shimadzu UV1601 spectrophotometer and a quartz cuvette of 0.1 cm path length. For exposing the negative charges of the quartz silicate groups (and therefore emulate the negative charge density of Au/MPS surface) the cuvette was treated for 20 min in an ultrasound bath with 1.0% w/v NaOH solution (in 59% v/v ethanol aqueous solution).

Scanning electron microscopy (SEM) images were obtained with a Field Emission Gun Scanning Electron Microscope (FE-SEM, Zeiss, ΣIGMA model).

The FTIR spectra were obtained with a 200X-ATR-V (Interspectrum) spectrophotometer using an ATR Miracle cell with Ge crystal window. Raman spectra were acquired with a LABRAM-HR Horiba Jobin-Yvon confocal microscope Raman system. The laser excitation and power were 632.8 nm (He−Ne) and 1.7 mW, respectively. Dynamic light scattering (DLS) and ζ-potential measurements were performed using a Beckman Coulter Delsa Nano C equipment. Thermogravimetric (TGA) measurements were carried out with a Shimadzu DTG-60 thermoanalyzer, between 25 and 800 °C (heat rate: 10 °C min^{-1}) under N$_2$ atmosphere.

SPR measurements were done with a single channel AUTOLAB SPRINGLE instrument (Eco Chemie). The SPR sensor disks (BK 7) were mounted on a hemicylindrical lens through index-matching oil to form the base of a cuvette. Sample solutions (60 μL) were injected manually into the cuvette. The measurements were carried out under non-flow liquid conditions at (25 ± 1) °C.

Scanning electrochemical microscopy (SECM) images were obtained with a CHI900 bipotentiostat (CHInstruments) using a home-made carbon fiber (diameter ~ 10 μm) as the ultramicroelectrode (UME) probe. SECM feedback mode was selected to obtain images of each modified surface using a 5.00 × 10^{-4} M ferrocene methanol (FcOH) solution. The UME and the substrate potentials were held at 0.500 V and 0.000 V during the acquisition of the images and the UME scan rate was 10.0 μm s^{-1}. The SECM surface plots are depicted by normalizing the current of the UME at the surface (i$_T$) with the steady-state current of the UME positioned far from the substrate (i$_{T,\infty}$).

Electrochemical experiments were performed with an Autolab PGSTAT 128 N potentiostat (Metrohm Autolab B.V.) equipped with a FRA 32 M module. Cyclic voltammetry (CV) experiments were carried out at a scan rate of $v = 0.050$ V s^{-1}. Electrochemical impedance spectroscopy (EIS) was conducted using 2.00×10^{-3} M quinone (Q)/hydroquinone (H$_2$Q) solution as redox probe (prepared in 0.100 M phosphate buffer solution pH 7.40) at open circuit potential (o.c.p., c.a. 0.070 V), with a potential amplitude of 10 mV from 10^5 to 10^{-2} Hz. Gold disk electrodes of 2 mm diameter (CHInstruments 101) were used as substrate during the electrochemical experiments. A platinum wire and an Ag/AgCl/NaCl (3 M) electrode (Model RE-5B, BAS) were used as counter and reference electrodes, respectively. The reported potentials are referred to this reference electrode. All experiments were performed at room temperature.

3. Results and discussion

3.1. Characterization of GO, GO-CHIT and RGO-CHIT

Fig. 1A depicts the FTIR spectra of CHIT, GO, GO-CHIT and RGO-CHIT. CHIT spectrum shows two characteristic bands at 1650 (amide I) and 1592 cm^{-1} (amide II), corresponding to the C=O stretching and N−H deformation, respectively. The bands around 1450−1200 and 1200-900 cm^{-1} correspond to C−H and O−H deformations and C−O tensions, respectively. GO spectrum displays bands at 1734 cm^{-1} (C=O stretching at GO borders), 1626 cm^{-1} (conjugated C=C stretching), 1169 cm^{-1} (phenol C−O stretching), and 1049 cm^{-1} (epoxy C−O−C stretching). The covalent modification of GO with CHIT shifts the amide I and II bands to lower wavenumbers (1639 cm^{-1} and 1544 cm^{-1}, respectively) due to the new amide bonds formed between NH$_2$ groups of CHIT and COOH residues of GO. The band corresponding to C=O bonds of GO still appears in the spectrum of GO-CHIT (shifted to 1721 cm^{-1}) indicating that, after the covalent modification, some carboxylic groups remained unreacted. The spectrum of RGO-CHIT shows the amide I and amide II bands (at 1643 and 1540 cm^{-1}) while the one corresponding to the unbonded C=O groups disappears as a consequence of the reduction with NaBH$_4$ [32].

Fig. 1B displays the TGA curves for CHIT, GO, GO-CHIT and RGO-CHIT. The three profiles show a weight loss around 100 °C is associated to the removal of water ab/adsorbed in the samples. The
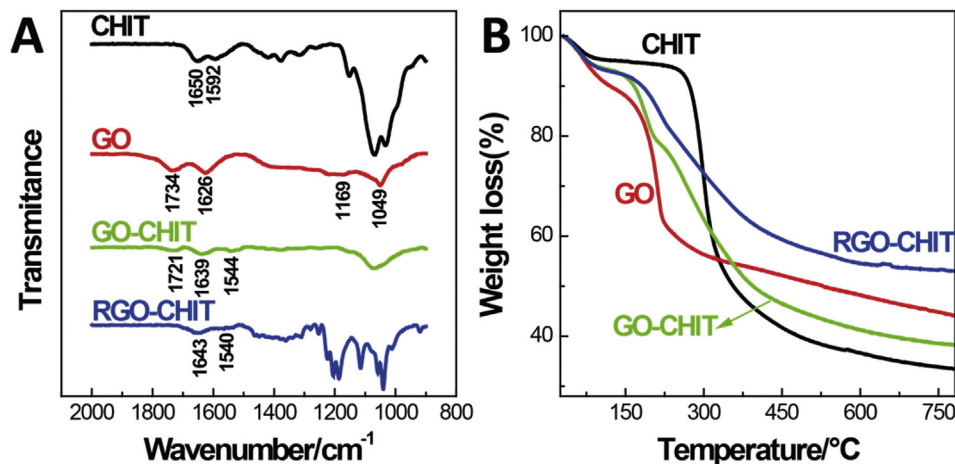
Fig. 1. FTIR spectra (**A**) and TGA curves (**B**) for CHIT (—), GO (——), GO-CHIT (——), and RGO-CHIT (——).

TGA curve for CHIT shows a 60% weight loss at 302 °C related to the thermal and oxidative decomposition of the polymer backbone [33]. The TGA profile for GO displays a mass loss of 33% at 211 °C which is associated to the pyrolysis of labile oxygen groups [34,35]. Both processes can be clearly discriminated in the derivative TGA curves presented in Fig. S2. The higher thermal stability evidenced by the lower mass loss at c.a. 210 °C and the weight loss at 280 °C observed in the TGA profile for GO-CHIT (decomposition of CHIT) are clear indications of the covalent functionalization of GO with CHIT. The spectrum of RGO-CHIT shows a lower weight-loss mass at 210 °C due to the partial removal of oxygen-containing- groups after the reduction of GO-CHIT and the corresponding contribution around 300 °C due to CHIT.

The comparison of the UV–Vis spectra for GO, GO-CHIT and RGO-CHIT provides additional evidences of the covalent modification of GO with CHIT and further reduction of GO (Fig. S3). The spectrum of GO displays two extinction bands at 234 and 305 nm, corresponding to the $\pi \rightarrow \pi^{*}$ transition of C=C conjugate bonds and C=O bonds, respectively [36]. The covalent attachment of CHIT to GO changes the dielectric constant of GO surroundings, upshifting the extinction bands of GO-CHIT spectrum by c.a. 9 nm. Upon the reduction to RGO-CHIT, the band corresponding to C=C bonds presents a bathochromic shift (to 260 nm) as π conjugation increases [36].

Figure S4 displays the Raman spectra for GO, GO-CHIT and RGO-CHIT and Table S1 summarizes the wavenumbers and intensity ratio for D and G bands. The covalent modification of GO and RGO with CHIT promotes the stability of the dispersions by preventing the re-stacking of the sheets, producing a downshift of the 2D band [37,38] of GO-CHIT and RGO-CHIT compared to GO. Upon reduction of GO-CHIT, D and G bands shift to lower wavenumbers due to restauration of graphitic C sp^2 lattice [34]. The increment of I_D/I_G ratio from GO-CHIT to RGO-CHIT (Table S1), reveals that upon treatment of GO-CHIT with $NaBH_4$ RGO-CHIT sp^2 domains size increases. As stated by Ferrari et al. [39,40], I_D/I_G decreases when $sp2$ carbon hexagonal structure starts to disappear.

### 3.2. Characterization of gold surfaces modified with dispersions of GO, GO-CHIT and RGO-CHIT and BSA

In the previous section we have demonstrated the effective covalent functionalization of GO with CHIT and further reduction to obtain RGO-CHIT. In this section we discuss the non-covalent immobilization of GO, GO-CHIT and RGO-CHIT at Au/MPS and the

covalent binding of the model protein, BSA, at the resulting Au-modified surfaces.

Fig. 2 depicts the SPR profiles obtained during the non-covalent immobilization of PDDA and GO (A), GO-CHIT (B) and RGO-CHIT (C) at Au/MPS, and the covalent attachment of BSA at each of the resulting platforms. The fast increase of SPR angle (θ_{SPR}) observed after the immobilization of the different grapheneous materials either to the positively charged PDDA (A) or to the negatively charged MPS (B and C), is indicative of a rapid and efficient adsorption. The interaction of the different platforms (Au/MPS/PDDA/GO, Au/MPS/GO-CHIT and Au/MPS/RGO-CHIT) with 1.00 mg mL^{-1} BSA also produces an important and fast increase of θ_{SPR} as a consequence of the covalent attachment of the protein to the carboxylic groups of GO through EDC/NHS chemistry (A) or to the amine groups of CHIT through the use of Glut (B and C). The change in the SPR angle before and after the attachment of BSA and careful washing of the surface ($\Delta\theta_{SPR}$), is related to the mass of protein immobilized at the surface [41]. Therefore, these $\Delta\theta_{SPR}$ let us to obtain the surface coverages of the protein (Γ_{BSA}) at the different platforms, being 8.21×10^{-12}, 3.14×10^{-12} and 4.46×10^{-12} mol cm^{-2} at Au/MPS/PDDA/GO, Au/MPS/GO-CHIT and Au/MPS/RGO-CHIT, respectively.

The construction of the different architectures was also evaluated by electrochemical techniques using FcOH as redox marker. Fig. 3A displays the peak potential separation (ΔE_p) for 5.00×10^{-4} M FcOH obtained from CV experiments performed after each step during the non-covalent immobilization of GO, GO-CHIT and RGO-CHIT at Au/MPS and the covalent attachment of BSA at the different platforms. CVs were performed at a scan rate of 0.050 V s^{-1} and are shown in Fig. S5. Upon the modification of Au with MPS, ΔE_p increases because of surface blockage produced by the thiol. The adsorption of PDDA at Au/MPS generates a positively charged film that electrostatically repels the oxidation product of FcOH, FcOH$^{\bullet+}$, generating an increment of ΔE_p. The self-assembly of GO at Au/MPS/PDDA produces the opposite effect due to the screening of PDDA positive charges by GO. At variance with the immobilization of GO at Au/MPS/PDDA, the assembly of GO-CHIT at Au/MPS produces an increment of ΔE_p due to the blocking effect of the tethered-polymer. In the case of Au/MPS/RGO-CHIT, in spite of the presence of the polymer, the assembly of RGO-CHIT produces a decrease of ΔE_p, from (127 ± 4) mV to (93 ± 4) mV associated with the improvement in the charge transfer kinetics of the redox probe due to the restoration of the sp^2 character of the graphitic network after reduction of GO-CHIT with $NaBH_4$ [42]. The covalent
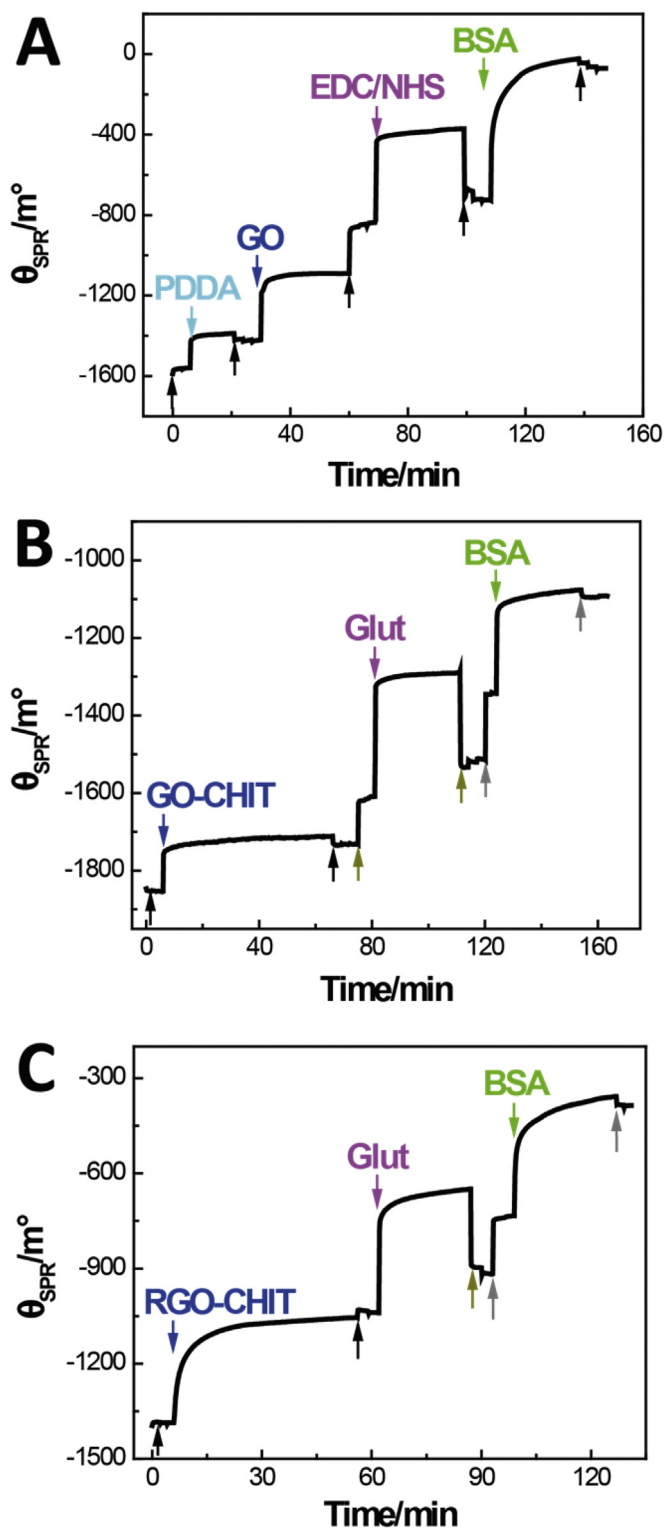
Fig. 2. A) Sensorgram obtained during the assembly of PDDA (↓) and GO (↓), activation with EDC/NHS (↓) and covalent immobilization of BSA (↓). Black arrows indicate the addition of phosphate buffer solution for rinsing the loosely bound materials. **B**) Sensorgram obtained during the assembly of GO-CHIT (↓), coupling with Glut (↓) and covalent immobilization of BSA (↓). The other arrows indicate the addition of phosphate buffer solution (↓), 1% v/v acetic acid (↓) and 0.200 M acetic acid solution pH 5.00 (↓) for rinsing the loosely bound materials. **C**) Sensorgram obtained during the assembly of RGO-CHIT (↓), coupling with Glut (↓) and covalent immobilization of BSA (↓). The other arrows indicate the addition of phosphate buffer solution (↓), 1% v/v acetic acid (↓) and 0.200 M acetic acid solution pH 5.00 (↓) for rinsing the loosely bound materials.

immobilization of BSA at any of the three platforms sluggish the FcOH charge transfer, rising ΔE_p, effect that is more or less pronounced depending on the amount of the model protein at the gold surface (as it will be discussed in the following paragraphs).

SECM feedback images were also used to evaluate the different architectures with FcOH as redox mediator. Fig. 3B shows the normalized currents ($i_T/i_{T,\infty}$) of UME at Au (a), Au/MPS/PDDA (b) and Au/MPS/PDDA/GO (c). The modification of Au with MPS and PDDA produces a decrease in the normalized currents due to the presence of the thiol and the positive layer of PDDA. The adsorption of GO at Au/MPS/PDDA restores $i_T/i_{T,\infty}$ to values close to bare Au electrode. SECM surface plot of Fig. 3C displays the profiles of the normalized currents for Au (a) and Au/MPS/GO-CHIT (b). As in the case previously described, the platform shows a relatively homogeneous local electroactivity although, at variance with the immobilization of GO at Au/MPS/PDDA, the incorporation of GO-CHIT produces a decrease in $i_T/i_{T,\infty}$ compared to bare Au, due to the blocking effect of the CHIT polymeric chains, in agreement with the voltammetric results previously described. Unlike the relatively smooth response obtained for Au/MPS/PDDA/GO and Au/MPS/GO-CHIT, the SECM profile of Au/MPS/RGO-CHIT (Fig. 3D) reveals areas with considerably different electroactivity, with $i_T/i_{T,\infty}$ values lower and higher than that for bare Au, demonstrating a non-homogeneous distribution of RGO-CHIT on the surfaces. The average $i_T/i_{T,\infty}$ values are higher than that obtained with bare Au which is in consonance with the improvement observed in the voltammetric experiments after incorporation of RGO-CHIT. In conclusion, SECM and CV results showed that, from the electrochemical point of view, the most reactive surface is Au/MPS/RGO-CHIT mainly due to the characteristics of RGO.

3.3. Effect of the pH of the grapheneous materials-dispersions on the construction of the platforms

To facilitate the understanding of the immobilization of BSA at Au/MPS/PDDA/GO, Au/MPS/GO-CHIT and Au/MPS/RGO-CHIT and taking into account the acid-base characteristics of GO and CHIT, we studied the effect of the pH used to prepare the nanomaterials dispersions on the dispersability and stability of GO, GO-CHIT and RGO-CHIT.

Fig. 4 displays the variation of the hydrodynamic radius and ζ-potential as a function of the pH of the dispersions. GO colloidal dispersions are charge-stabilized [43,44], therefore, at low pHs the carboxylic groups of GO are protonated, decreasing the hydrophilicity of the sheets [45], inducing aggregation and increase in the radius (Fig. 4A). As the pH increases up to pH 8.00, the deprotonation of the carboxylic groups produces a decrease of ζ-potential and, therefore, of the hydrodynamic radius, due to the increase of GO negative charges density. The minimum in ζ-potential and hydrodynamic radius observed at pH 8.00 is associated with the screening of the negative charges of GO while adjusting the pH [44–46] as a result of the increase in the ionic strength. Unlike GO, GO-CHIT and RGO-CHIT have positive values of ζ-potentials (Fig. 4B) since the colloidal charge-stabilization comes from the ammonium groups of CHIT polymeric chains (pKa_{CHIT} ranges between 4 and 6 depending on the length and degree of deacetylation [47,48]). When the pH increases, the ζ-potentials become lower and the hydrodynamic radius increases due to the deprotonation of the $-NH_2$ residues of CHIT that decreases the positive charge density of the colloid and the polymer chains roll up and form aggregates through van de Waals and hydrogen bonding interactions. In fact, above pH 6.00 the dispersion is not stable and it precipitates once suspended the ultrasound treatment.

The influence of the pH of the grapheneous materials dispersions on their assembly at Au/MPS was evaluated through the
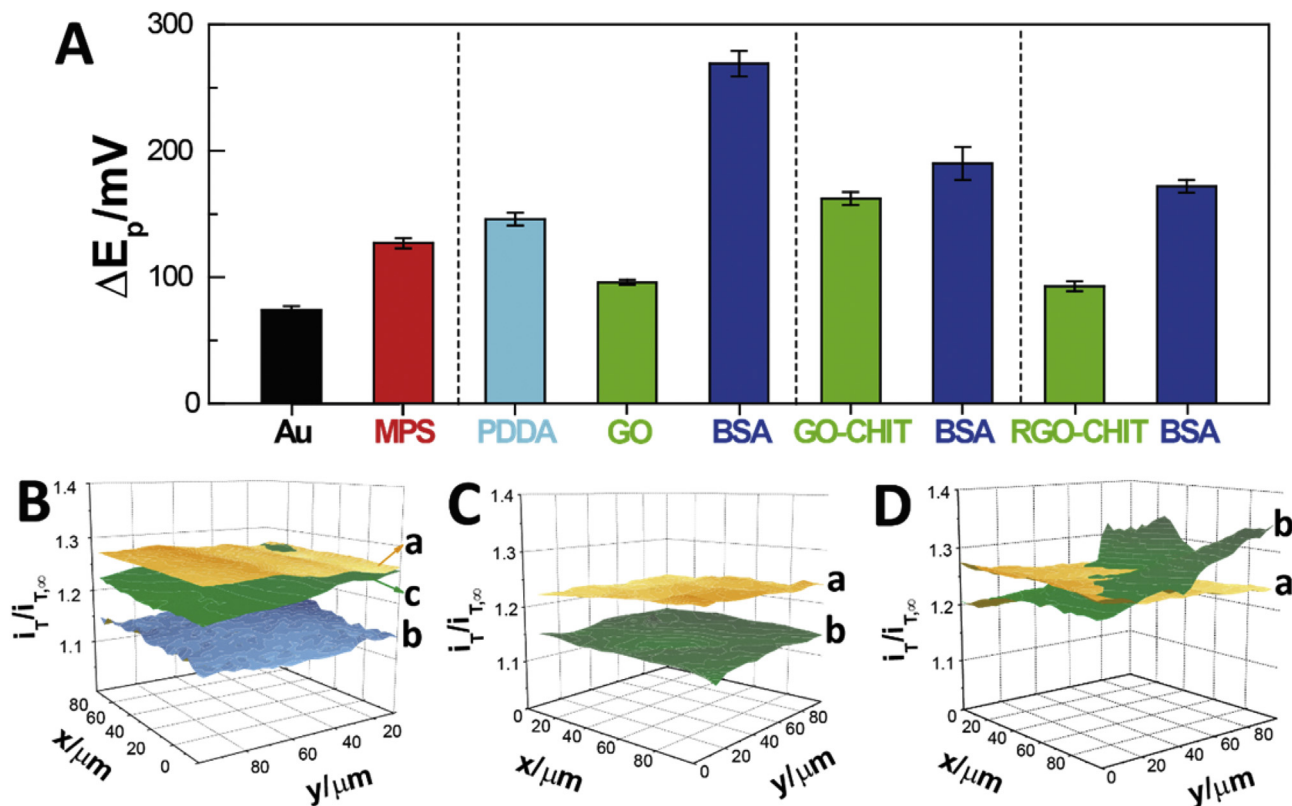
Fig. 3. A) Peak potential difference (ΔE_p) obtained from CV experiments using 5.00×10^{-4} M FcOH as redox probe. The first part corresponds to the modification of Au with MPS, common for the three strategies. The second, third and fourth blocks of bars are for the modification of Au/MPS with PDDA/GO, GO-CHIT and RGO-CHIT and the subsequent binding of the model protein, respectively. Supporting electrolyte: 0.100 M phosphate buffer solution 7.40. $v = 0.050$ V s^{-1}. **B**) SECM feedback plots obtained at Au (**a**), Au/MPS/PDDA (**b**), and Au/MPS/PDDA/GO (**c**). **C**) SECM feedback plots obtained at Au (**a**), and Au/MPS/GO-CHIT (**b**). **D**) SECM feedback plots obtained at Au (**a**), and Au/MPS/RGO-CHIT (**b**). SECM conditions: $E_{UME} = 0.500$ V, $E_{substrate} = 0.000$ V, scan rate $= 10.0$ μm s^{-1}, redox probe $= 5.00 \times 10^{-4}$ FcOH solution, supporting electrolyte $= 0.100$ M phosphate buffer solution 7.40.

resulting local electrochemical properties. Fig. 5A shows SECM surface plots for Au/MPS/PDDA after the assembly of GO dispersions of different pHs. As the pH of the dispersion increases, there is an increment in the normalized currents up to pH 8.00, to decrease thereafter. This maximum is connected with the minimum in GO ζ-potential profile and is related to a higher density of carboxylate groups and a better GO dispersion. Fig. 5B displays the SECM images for Au/MPS/GO-CHIT using GO-CHIT dispersions of different pHs. At more acidic pHs, the normalized currents are smaller than that obtained at bare Au as a consequence of the blocking effect of the polymer and the presence of protonated amine residues. As the pH of the dispersion increases the normalized currents also increase due to the deprotonation of CHIT (although remain smaller than the normalized current at bare Au electrode). SECM surface plots for RGO-CHIT (Fig. 5C) shows that when the dispersion is prepared at pHs close to the pka of CHIT, lower and non-homogeneous $i_T/i_{T,\infty}$ values are observed, due to the poor dispersability of RGO-CHIT and formation of aggregates at the surface. Conversely, the profile at pH 2.00 presents $i_T/i_{T,\infty}$ values higher than those for bare Au and shows a more homogeneous response since the protonated nature of CHIT grafted chains facilitates the interaction with the underlying negative charges of Au/MPS. These results demonstrate that, even considering the blocking effect of the CHIT that modifies RGO, when the dispersability of RGO-CHIT is optimal (pH < pKa), the electroactive behavior of the RGO is the one that prevails.

Since the variation in the pH of the grapheneous materials dispersions produces important changes in the morphology and electrochemical reactivity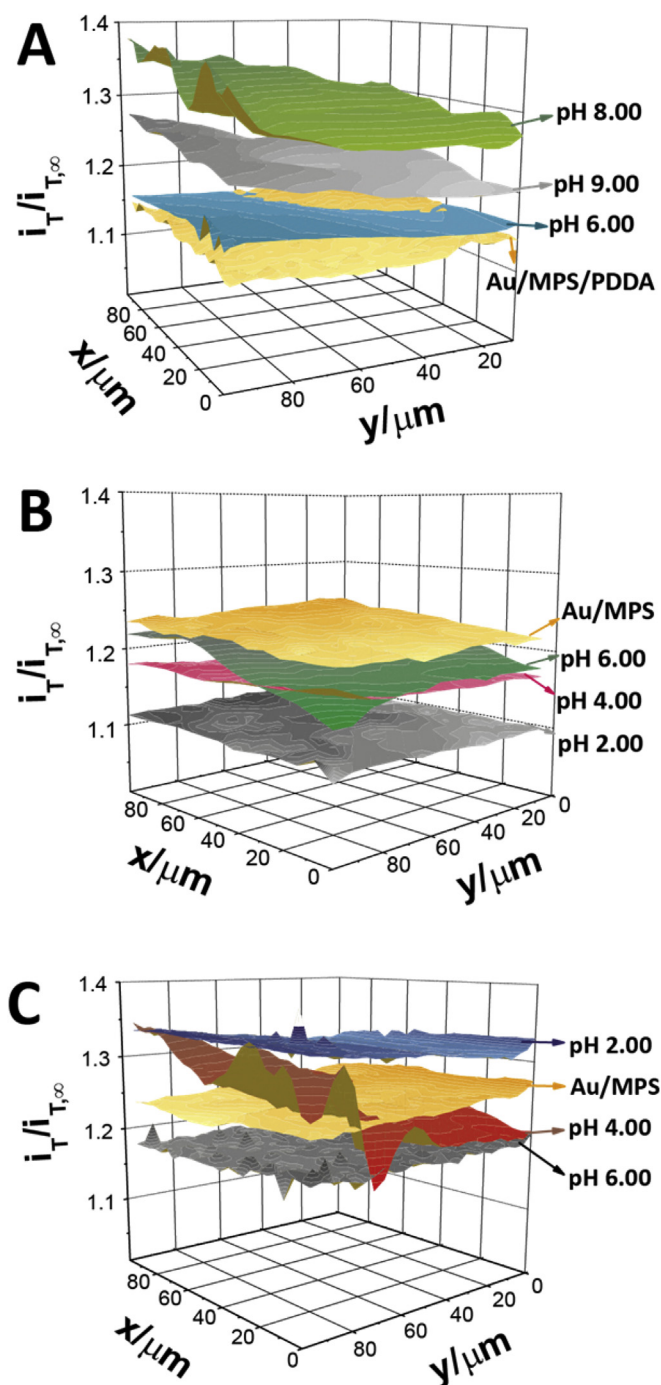 of the platforms, we also evaluated the influence of the pH of the dispersions on the immobilization of BSA. Fig. 6A shows the effect of the pH of GO dispersions assembled at Au/MPS/PDDA on Γ_{BSA} (obtained from SPR experiments). The higher amount of GO carboxylate groups obtained with the increase of the dispersion pH increases the number of protein anchoring points producing an increment in Γ_{BSA} up to pH 8.00. At pH > 8.00 Γ_{BSA} decreases in the same way as the ζ-potential behavior (Fig. 4A). In the case of GO-CHIT (Fig. 6B), the increase of pH produces a decrease in the amount of BSA attached to Au/MPS/GO-CHIT due to a lower amount of anchoring points as a consequence of the poor dispersability of RGO-CHIT, as it was previously described. The profile of Γ_{BSA} versus pH obtained for the assembling at Au/MPS/RGO-CHIT (Fig. 6C), is similar to the one observed for Au/MPS/GO-CHIT.

It is widely known that EIS is a powerful tool for the detection of protein binding processes at electrodes surfaces. Hence, we performed EIS experiments for Au/MPS/PDDA/GO (Fig. S6), Au/MPS/GO-CHIT (Fig. S7) and Au/MPS/RGO-CHIT (Fig. S8) before and after the assembling of BSA using 2.00×10^{-3} M Q/H$_2$Q as redox probe (prepared in a 0.100 M phosphate buffer solution pH 7.40). This couple is adsorbed at sp^2 carbon during electron transfer [49] and, in this way, is sensitive to the surface blockage/coverage. Fig. 6D depicts the total resistances (R) obtained at Au/MPS/PDDA/GO (orange bars) and Au/MPS/PDDA/GO/BSA (purple bars), from the corresponding EIS spectra fittings (equivalent circuits and a short explanation of how R was obtained can be found in the Supporting Information). In consonance with previous results, the smallest value of R is obtained when the pH of GO dispersion is 8.00 because, even when GO is an electrical insulator, its k_0 is higher
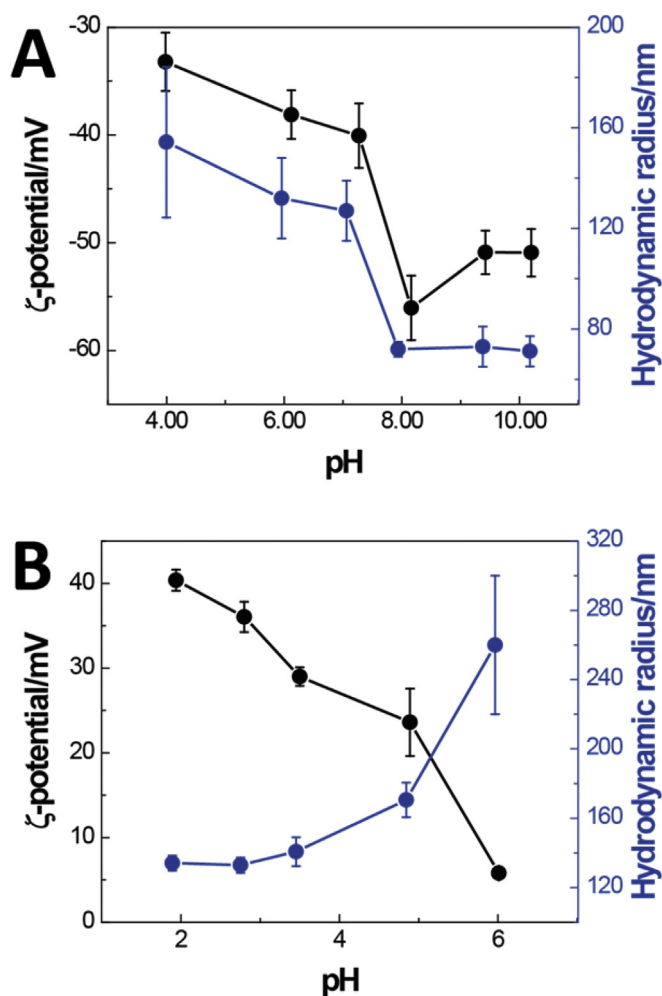
Fig. 4. GO (**A**) and GO-CHIT/RGO-CHIT (**B**) dispersion pH dependence of ζ-potential (●, left axis) and hydrodynamic radius (●, right axis).

Fig. 5. A) SECM surface plots obtained at Au/MPS/PDDA and Au/MPS/PDDA/GO after the assembly of 0.50 mg mL^{-1} GO dispersions at various pH: 6.00, 8.00 and 9.00. **B**) SECM surface plots obtained at Au and Au/MPS/GO-CHIT after the assembly of 0.50 mg mL^{-1} GO-CHIT dispersions at various pH: 6.00, 4.00 and 2.00. **C**) SECM surface plots obtained at Au and Au/MPS/RGO-CHIT after the assembly of 0.50 mg mL^{-1} RGO-CHIT dispersions at various pH: 6.00, 4.00 and 2.00. Table S2, S3 and S4 (in the supporting information) shows the average values for each condition of Au/MPS/PDDA/GO, Au/MPS/GO-CHIT and Au/MPS/RGO-CHIT, respectively. SECM conditions as in Fig. 3B–D.

than that of the subjacent Au/MPS/PDDA layer. The covalent immobilization of BSA at Au/MPS/PDDA generates an increment in R at all pHs due to the surface blockage and reaction kinetics hindering (purple bars). Therefore, at pH 8.00 the maximum mass loading of BSA generates the highest increment in R for Q/H$_2$Q. The variation of R for Q/H$_2$Q before and after BSA immobilization was also evaluated at Au/MPS/GO-CHIT (Fig. 6E). At pH 2.00, even when GO-CHIT is an electrical insulator, since its k$_0$ is higher than that for Au/MPS layer, the R is the smallest and the main responsible is the assembly of a larger amount of nanomaterial under these conditions (orange bars). As the pH of the GO-CHIT assembled dispersion increases, the amount of immobilized dispersion is reduced and the total R increases due to the incomplete coverage of the passivated Au/MPS surface. The assembly of BSA produces important changes in R at lower pHs because the density of amino groups and the amount of BSA linked to the platform are maximum and generates the largest difference in R (Fig. 6E, purple bars). As the pH increases, the blockage of the surface by the aggregation of CHIT functionalized nanomaterials is the most important effect (compared to the blocking effect of the protein) and the change in R is smaller. As the pH increases, the presence of lower amount of GO-CHIT at the surface and, consequently, lower protein coverage, produce smaller changes in R. Regarding RGO-CHIT (Fig. 6F, orange bars), the profile of R with the pH of the assembled dispersion is similar to the one obtained for Au/MPS/GO-CHIT although the absolute values are

smaller because of the higher C sp^2/sp^3 ratio and conductive nature of RGO. The covalent immobilization of BSA makes the total R to increase due to surface blockage (Fig. 6F, purple bars). Since the platform assembled at pH 2.00 is the one with the highest amount of RGO-CHIT (and largest density of −NH$_2$ groups), it is the one with
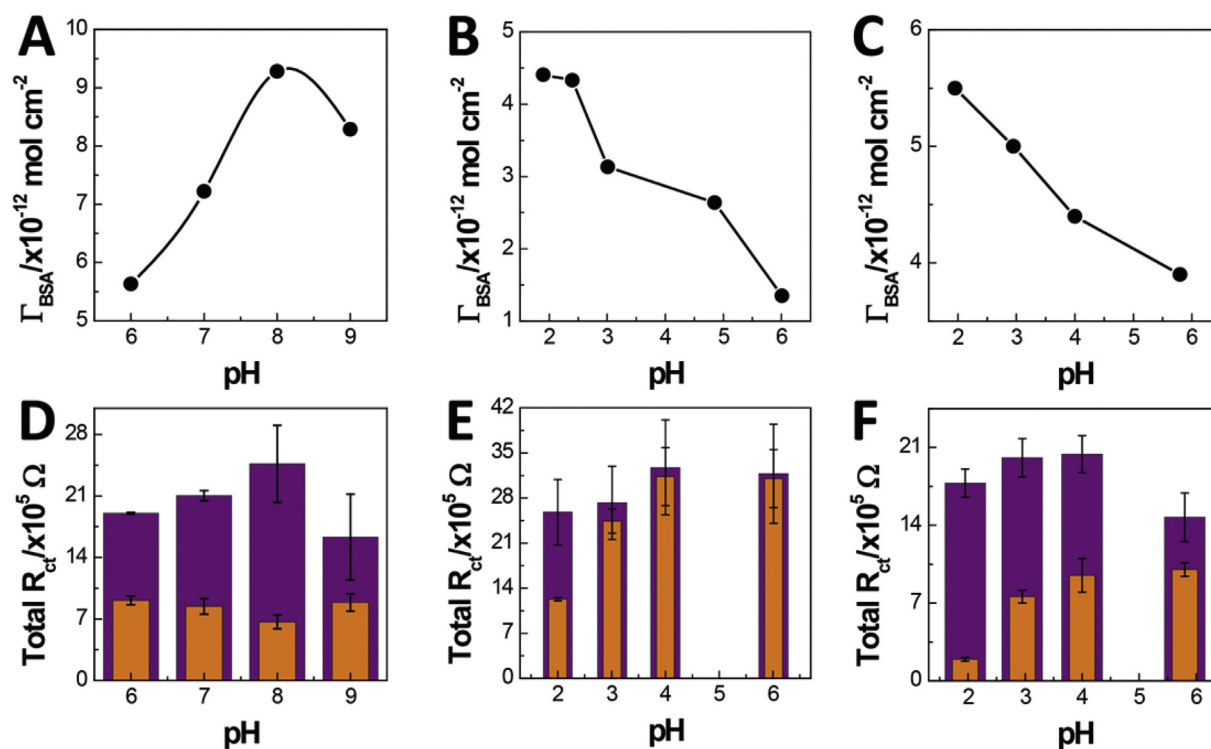
Fig. 6. First row. BSA surface coverages (Γ_{BSA}) as a function of graphene-derived dispersion pH assembled at Au/MPS for GO (**A**), GO-CHIT (**B**) and RGO-CHIT (**C**). Γ_{BSA} was obtained from independent SPR experiments at each condition, through $\Delta\theta_{SPR}$ due to the covalent immobilization of the model protein. **Second row.** Resistance dependency with graphene-derived dispersion pH assembled at Au/MPS for GO (**D**), GO-CHIT (**E**) and RGO-CHIT (**F**). The total resistances were obtained by fitting the EIS spectra in 2.00×10^{-3} M Q/H$_2$Q solution with a capillary membrane-equivalent circuit. Orange bars correspond to R$_{ct}$ values before BSA covalent immobilization at the platforms and purple bars, to the values after tethering the model protein. EIS spectra and equivalent circuit used to fit the data are depicted in Figs. S6–8, in the Supporting Information. Measurement conditions: E$_{dc}$ = o.c.p. (c.a. 0.070 V), amplitude = 10 mV, frequency range = 10^5 to 10^{-2} Hz, supporting electrolyte = 0.100 M phosphate buffer solution 7.40.

the largest change in R. In summary, lower pHs favor the assembly of RGO-CHIT at Au/MPS and the attachment of BSA at Au/MPS/RGO-CHIT, amplifying the changes in R.

3.4. Final comparison: grapheneous material versus transduction of the model protein assembly

Table 1 presents the most relevant results obtained for the different platforms regarding SECM surface reactivity, SEM images, grapheneous-materials coverages, Γ_{BSA}, and the percentage of increase of R.

The first row of the table displays SEM images of the different platforms. They reveal that Au/MPS/PDDA/GO is the platform that possesses the most homogeneous coverage of the surface. However, in all cases is possible to distinguish the graphenoid sheets with their jagged edges and irregular facets. A good interconnection between the different graphenoid sheets is also evident for the three surfaces, in agreement with the SECM surface plots presented in the second row. The SECM plots show the highest i$_T$/i$_{T,\infty}$ for Au/MPS/RGO-CHIT, demonstrating that among the three platforms, it is the most electroactive platform due to restoration of C sp^2 network after the reduction with NaBH$_4$. This is supported by the fact that R$_{ct}$ is the lowest for Au/MPS/RGO-CHIT platform (note the resistance values of Fig. 6D–F).

The coverage values calculated by UV–Vis spectroscopy (third row of Table 1) are in agreement with the coverages shown in SEM images: Au/MPS/GO-CHIT and Au/MPS/RGO-CHIT contain about half of nanomaterial than Au/MPS/PDDA/GO, and they present almost the half of Γ_{BSA}, clearly demonstrating the direct connection between nanomaterial coverage and protein loading.

Consequently, for the development of biosensors where the recognition layer is a protein and the detection method is direct and depends on the amount of immobilized protein (SPR, for example), one has to optimize how the assembly conditions/methodology affect the platform's protein loading. For our case, as Au/MPS/PDDA/GO has the highest availability of protein anchoring points, is the chosen one.

The last row of Table 1 presents the change of R for Q/H$_2$Q before and after BSA immobilization. The platform that possesses the highest change is Au/MPS/RGO-CHIT, however, it is not associated with the amount of immobilized nanomaterial or Γ_{BSA}, since Au/MPS/PDDA incorporates about twice as much GO than RGO-CHIT at Au/MPS, and Γ_{BSA} is almost the half of the one obtained at Au/MPS/PDDA/GO. The higher change in the R is due to the conductive nature of RGO-CHIT that makes it more sensitive to surface blockage. Therefore, for the development of biosensors where the transduction is based on the changes of the electrochemical properties of an inner-sphere redox marker (as in the case of EIS), one has to optimize the methodology to maximize the differences in charge transfer without and with the protein insulating layer. In our analyzed systems, this accomplished with the Au/MPS/RGO-CHIT platform.
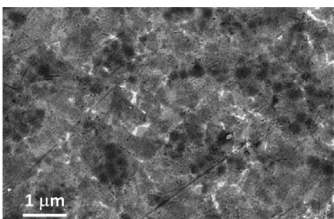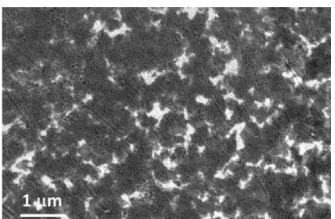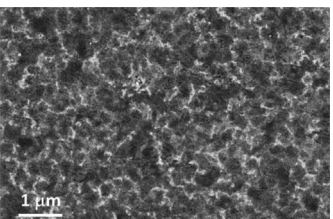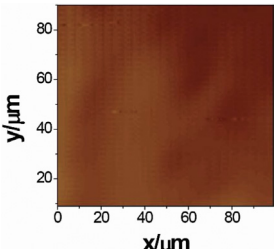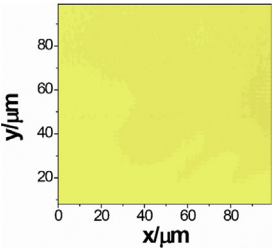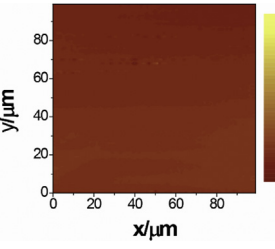
4. Conclusions

We reported here the importance of performing a rational selection of the graphene-derived materials (GO, GO-CHIT or RGO-CHIT) and the conditions for their incorporation at gold surfaces for the successful immobilization of BSA (taken as model protein). We demonstrated the importance of the pH of the grapheneous

Table 1
General comparison of the most relevant results for each strategy: Au/MPS/PDDA/GO, Au/MPS/GO-CHIT, and Au/MPS/RGO-CHIT.

	PDDA/GO	GO-CHIT	RGO-CHIT
Surface morphology (SEM)			
Surface electroactivity (SECM)[a]			
Nanomaterial surface coverage[b]/mg cm^{-2}	6.90×10^{-4}	3.78×10^{-4}	3.64×10^{-4}
Γ_{BSA}/mol cm^{-2}	9.18×10^{-12}	4.33×10^{-12}	5.50×10^{-12}
R percentage increase[c]	269	110	821

[a] SECM images depicted in previous sections, presented in 2D.

[b] Obtained through the assembly of PDDA/GO, GO-CHIT or RGO-CHIT at an activated quartz cuvette. The assembly was performed in the same fashion as over the Au substrates. Nanomaterial coverages were obtained after recording the UV—Vis spectra, using the extinction coefficients ε previously calculated from dispersions of known concentrations at the maximum of absorption. ε(GO, 230 nm) = 49.0 mL mg^{-1} cm^{-1}. ε(GO-CHIT, 232 nm) = 22.4 mL mg^{-1} cm^{-1}. ε(RGO-CHIT, 258 nm) = 22.0 mL mg^{-1} cm^{-1}.

[c] Calculated as [R(with BSA) − R(without BSA)]*100/R(without BSA).

materials dispersions in two crucial aspects: i) the amount of nanomaterial and BSA attached at the gold surfaces, and ii) the electrochemical and plasmonic properties of the resulting platforms. The other critical aspect we studied here, intimately related to the amount of nanomaterial and protein coverage, is the importance of performing a rational selection of the technique used for transducing the signal according to the characteristics of the platform. These results demonstrated that the knowledge of basic information of a nano-bio-platform based on grapheneous-materials and proteins, going from the immobilization of the grapheneous-nanomaterial step to the final transduction scheme is essential to further obtain biosensing platforms with good analytical performance.

For our system (immobilization of BSA at Au/MPS/PDDA/GO, Au/MPS/GO-CHIT and Au/MPS/RGO-CHIT) we demonstrated that, if the detection method depends on the direct quantification of the amount of BSA immobilized at the platform, the use of GO is the best option while if the detection mode depends on the changes in the electrochemical response of a redox marker, the use of RGO is the most appropriate.

Acknowledgments

Appendix A. Supplementary data

Supplementary data related to this article can be found at https://doi.org/10.1016/j.electacta.2017.10.184.

References

[1] R.S. Edwards, K.S. Coleman, Graphene synthesis: relationship to applications, Nanoscale 5 (2013) 38—51, https://doi.org/10.1039/C2NR32629A.

[2] P.T. Yin, S. Shah, M. Chhowalla, K.-B. Lee, Design, synthesis, and characterization of graphene—nanoparticle hybrid materials for bioapplications, Chem. Rev. 115 (2015) 2483—2531, https://doi.org/10.1021/cr500537t.

[3] S.R. Shin, Y.-C. Li, H.L. Jang, P. Khoshakhlagh, M. Akbari, A. Nasajpour, et al., Graphene-based materials for tissue engineering, Adv. Drug Deliv. Rev. 105 (Part) (2016) 255—274. https://doi.org/10.1016/j.addr.2016.03.007.

[4] C.A. Ubani, M.A. Ibrahim, M.A.M. Teridi, K. Sopian, J. Ali, K.T. Chaudhary, Application of graphene in dye and quantum dots sensitized solar cell, Sol. Energy 137 (2016) 531—550. https://doi.org/10.1016/j.solener.2016.08.055.

[5] W. Lv, Z. Li, Y. Deng, Q.-H. Yang, F. Kang, Graphene-based materials for electrochemical energy storage devices: opportunities and challenges, Energy Storage Mater 2 (2015) 1—32, https://doi.org/10.1016/j.ensm.2015.10.002.

[6] S.K. Vashist, J.H.T. Luong, Recent advances in electrochemical biosensing schemes using graphene and graphene-based nanocomposites, Carbon N. Y. 84 (2015) 519—550. https://doi.org/10.1016/j.carbon.2014.12.052.

[7] A. Karimi, A. Othman, A. Uzunoglu, L. Stanciu, S. Andreescu, Graphene based enzymatic bioelectrodes and biofuel cells, Nanoscale 7 (2015) 6909—6923, https://doi.org/10.1039/C4NR07586B.

[8] A. Criado, M. Melchionna, S. Marchesan, M. Prato, The covalent functionalization of graphene on substrates, Angew. Chem. Int. Ed. 54 (2015) 10734—10750, https://doi.org/10.1002/anie.201501473.

[9] A. Rabti, N. Raouafi, A. Merkoçi, Bio(Sensing) devices based on ferrocene—functionalized graphene and carbon nanotubes, Carbon N. Y. 108 (2016) 481—514. https://doi.org/10.1016/j.carbon.2016.07.043.

[10] X. Ji, Y. Xu, W. Zhang, L. Cui, J. Liu, Review of functionalization, structure and properties of graphene/polymer composite fibers, Compos. Part A Appl. Sci. Manuf. 87 (2016) 29—45. https://doi.org/10.1016/j.compositesa.2016.04.011.

[11] S.P. Lonkar, Y.S. Deshmukh, A.A. Abdala, Recent advances in chemical modifications of graphene, Nano Res. 8 (2014) 1039—1074, https://doi.org/10.1007/s12274-014-0622-9.

[12] J. Byun, Emerging frontiers of graphene in biomedicine, J. Microbiol. Biotechnol. 25 (2015) 145—151.

[13] Y. Fang, E. Wang, Electrochemical biosensors on platforms of graphene, Chem. Commun. 49 (2013) 9526—9539, https://doi.org/10.1039/C3CC44735A.

[14] H. Gao, H. Duan, 2D and 3D graphene materials: preparation and bioelectrochemical applications, Biosens. Bioelectron. 65 (2015) 404—419. https://doi.org/10.1016/j.bios.2014.10.067.

[15] J. Liu, Z. Liu, C.J. Barrow, W. Yang, Molecularly engineered graphene surfaces for sensing applications: a review, Anal. Chim. Acta 859 (2015) 1—19, https://

doi.org/10.1016/j.aca.2014.07.031.

[16] D.F. Báez, S. Bollo, A comparative study of electrochemical performances of carbon nanomaterial-modified electrodes for DNA detection. Nanotubes or graphene? J. Solid State Electrochem 20 (2016) 1059–1064, https://doi.org/10.1007/s10008-015-2997-2.

[17] T. Lee, S.H. Min, M. Gu, Y.K. Jung, W. Lee, J.U. Lee, et al., Layer-by-Layer assembly for graphene-based multilayer nanocomposites: synthesis and applications, Chem. Mater 27 (2015) 3785–3796, https://doi.org/10.1021/acs.chemmater.5b00491.

[18] Y. Gu, C. Ju, Y. Li, Z. Shang, Y. Wu, Y. Jia, et al., Detection of circulating tumor cells in prostate cancer based on carboxylated graphene oxide modified light addressable potentiometric sensor, Biosens. Bioelectron. 66 (2015) 24–31, https://doi.org/10.1016/j.bios.2014.10.070.

[19] J. Narayanan, M.K. Sharma, S. Ponmariappan, Sarita, M. Shaik, S. Upadhyay, Electrochemical immunosensor for botulinum neurotoxin type-E using covalently ordered graphene nanosheets modified electrodes and gold nanoparticles-enzyme conjugate, Biosens. Bioelectron. 69 (2015) 249–256, https://doi.org/10.1016/j.bios.2015.02.039.

[20] E.B. Bahadır, M.K. Sezgintürk, Applications of graphene in electrochemical sensing and biosensing, Trac. Trends Anal. Chem. 76 (2016) 1–14. https://doi.org/10.1016/j.trac.2015.07.008.

[21] Y. Song, Y. Luo, C. Zhu, H. Li, D. Du, Y. Lin, Recent advances in electrochemical biosensors based on graphene two-dimensional nanomaterials, Biosens. Bioelectron. 76 (2016) 195–212. https://doi.org/10.1016/j.bios.2015.07.002.

[22] S. Alwarappan, S. Boyapalle, A. Kumar, C.Z. Li, S. Mohapatra, Comparative study of single-, few-, and multilayered graphene toward enzyme conjugation and electrochemical response, J. Phys. Chem. C 116 (2012) 6556–6559, https://doi.org/10.1021/jp211201b.

[23] Y. Zhang, J. Zhang, X. Huang, X. Zhou, H. Wu, S. Guo, Assembly of graphene oxide-enzyme conjugates through hydrophobic interaction, Small 8 (2012) 154–159, https://doi.org/10.1002/smll.201101695.

[24] I. Macwan, M.D.H. Khan, A. Aphale, S. Singh, J. Liu, M. Hingorani, et al., Interactions between avidin and graphene for development of a biosensing platform, Biosens. Bioelectron. 89 (Part 1) (2017) 326–333. https://doi.org/10.1016/j.bios.2016.07.024.

[25] T. Wei, Z. Dai, Y. Lin, D. Du, Electrochemical immunoassays based on graphene: a review, Electroanalysis 28 (2016) 4–12, https://doi.org/10.1002/elan.201500461.

[26] A. Santos, P.R. Bueno, Glycoprotein assay based on the optimized immittance signal of a redox tagged and lectin-based receptive interface, Biosens. Bioelectron. 83 (2016) 368–378, https://doi.org/10.1016/j.bios.2016.04.043.

[27] P. Singh, SPR biosensors: historical perspectives and current challenges, Sensors Actuators B Chem. 229 (2016) 110–130. https://doi.org/10.1016/j.snb.2016.01.118.

[28] M. Puiu, C. Bala, SPR and SPR imaging: recent trends in developing nanodevices for detection and real-time monitoring of biomolecular events, Sensors 16 (2016) 870, https://doi.org/10.3390/s16060870.

[29] G.T. Hermanson, Zero-length crosslinkers, in: G.T. Hermanson (Ed.), Bioconjugate Tech, third ed., Academic Press, Boston, 2013, pp. 259–273. https://doi.org/10.1016/B978-0-12-382239-0.00004-2.

[30] C. Mokrani, J. Fatisson, L. Guérente, P. Labbé, Structural characterization of (3-mercaptopropyl)sulfonate monolayer on gold surfaces, Langmuir 21 (2005) 4400–4409, https://doi.org/10.1021/la047125s.

[31] G.T. Hermanson, Homobifunctional crosslinkers, in: G.T. Hermanson (Ed.), Bioconjugate Tech, third ed., Academic Press, Boston, 2013, pp. 275–298. https://doi.org/10.1016/B978-0-12-382239-0.00005-4.

[32] H.-J. Shin, K.K. Kim, A. Benayad, S.-M. Yoon, H.K. Park, I.-S. Jung, et al., Efficient reduction of graphite oxide by sodium borohydride and its effect on electrical conductance, Adv. Funct. Mater 19 (2009) 1987–1992, https://doi.org/10.1002/adfm.200900167.

[33] G.K. da R. Cortes, E.F.S. Vieira, A.R. Cestari, R.A. Chagas, Tetracycline release from chitosan/fish-scale-based membranes, J. Appl. Polym. Sci. 131 (2014) 39943, https://doi.org/10.1002/app.39943.

[34] S. Stankovich, D.A. Dikin, R.D. Piner, K.A. Kohlhaas, A. Kleinhammes, Y. Jia, et al., Synthesis of graphene-based nanosheets via chemical reduction of exfoliated graphite oxide, Carbon N. Y. 45 (2007) 1558–1565, https://doi.org/10.1016/j.carbon.2007.02.034.

[35] J. Shen, Y. Hu, C. Li, C. Qin, M. Ye, Synthesis of amphiphilic graphene nanoplatelets, Small 5 (2009) 82–85, https://doi.org/10.1002/smll.200800988.

[36] D. Li, M.B. Muller, S. Gilje, R.B. Kaner, G.G. Wallace, Processable aqueous dispersions of graphene nanosheets, Nat. Nanotechnol. 3 (2008) 101–105.

[37] A.C. Ferrari, J.C. Meyer, V. Scardaci, C. Casiraghi, M. Lazzeri, F. Mauri, et al., Raman spectrum of graphene and graphene layers, Phys. Rev. Lett. 97 (2006) 187401.

[38] J.M. Englert, C. Dotzer, G. Yang, M. Schmid, C. Papp, J.M. Gottfried, et al., Covalent bulk functionalization of graphene, Nat. Chem. 3 (2011) 279–286.

[39] A.C. Ferrari, J. Robertson, Interpretation of Raman spectra of disordered and amorphous carbon, Phys. Rev. B 61 (2000) 14095–14107.

[40] A. Jorio, R. Saito, G. Dresselhaus, M.S. Dresselhaus, Raman spectroscopy: from graphite to sp2 nanocarbons, in: Raman Spectrosc. Graphene Relat. Syst, WILEY-VCH Verlag GmbH & Co. KGaA, Weinheim, 2011, pp. 73–102, https://doi.org/10.1002/9783527632695.

[41] A. Kausaite, M. van Dijk, J. Castrop, A. Ramanaviciene, J.P. Baltrus, J. Acaite, et al., Surface plasmon resonance label-free monitoring of antibody antigen interactions in real time, Biochem. Mol. Biol. Educ. 35 (2007) 57–63, https://doi.org/10.1002/bmb.22.

[42] X. Zong, N. Kong, J. Liu, W. Yang, M. Cao, J.J. Gooding, The influence of graphene on the electrical communication through organic layers on graphite and gold electrodes, Electroanalysis 26 (2014) 84–92, https://doi.org/10.1002/elan.201300246.

[43] I. Chowdhury, M.C. Duch, N.D. Mansukhani, M.C. Hersam, D. Bouchard, Colloidal properties and stability of graphene oxide nanomaterials in the aquatic environment, Environ. Sci. Technol. 47 (2013) 6288–6296, https://doi.org/10.1021/es400483k.

[44] B. Konkena, S. Vasudevan, Understanding aqueous dispersibility of graphene oxide and reduced graphene oxide through pKa measurements, J. Phys. Chem. Lett. 3 (2012) 867–872, https://doi.org/10.1021/jz300236w.

[45] L.J. Cote, J. Kim, Z. Zhang, C. Sun, J. Huang, Tunable assembly of graphene oxide surfactant sheets: wrinkles, overlaps and impacts on thin film properties, Soft Matter 6 (2010) 6096–6101, https://doi.org/10.1039/C0SM00667J.

[46] J. Rong, M. Ge, X. Fang, C. Zhou, Solution ionic strength engineering as a generic strategy to coat graphene oxide (GO) on various functional particles and its application in high-performance lithium-sulfur (Li-S) batteries, Nano Lett. 14 (2014) 473–479, https://doi.org/10.1021/nl403404v.

[47] M. Rinaudo, Chitin and chitosan: properties and applications, Prog. Polym. Sci. 31 (2006) 603–632. https://doi.org/10.1016/j.progpolymsci.2006.06.001.

[48] H. Bao, Y. Pan, Y. Ping, N.G. Sahoo, T. Wu, L. Li, et al., Chitosan-functionalized graphene oxide as a nanocarrier for drug and gene delivery, Small 7 (2011) 1569–1578, https://doi.org/10.1002/smll.201100191.

[49] R.L. McCreery, Advanced carbon electrode materials for molecular electrochemistry, Chem. Rev. 108 (2008) 2646–2687, https://doi.org/10.1021/cr068076m.